KTH Industrial Engineering
and Management

Describing Interstitials in Close-packed Lattices: First-principles Study

Noura Al-Zoubi

Licentiate Thesis
Stockholm, Sweden 2011

Applied Materials Physics
Department of Materials Science and Engineering
Royal Institute of Technology

Materialvetenskap
ISRN KTH/MSE—11/03—SE+AMFY/AVH SE-100 44 Stockhlom
ISBN 978-91-7415-880-9 Sweden

Akademisk avhandling som med tillstånd av Kungliga Tekniska Högskolan framlaägges till offentlig granskning för avläggande av licentiatexamen, fredagen den 25 March 2011 kl 10.00 i konferensrummet, Materialvetenskap, Kungliga Tekniska Högskolan, Brinellvägen 23, Stockholm

Tryck: Universitetsservice US AB

Abstract

Describing interstitial atoms in simple mono-atomic close-packed metals or intermetallics is a straightforward procedure in common full-potential calculations. One establishes a sufficiently large supercell, introduces the interstitial impurity and performs the electronic structure and total energy calculation. Real systems, however, are rarely mono-atomic or ordered metals. In most of the cases, the matrix is a random or quasi-random mixture of several chemically and/or magnetically distinct components. Because of that a proper computational tool should incorporate advanced alloy theory and at the same time have sufficiently high accuracy to describe interstitial positions in close-packed solids. The purpose of the present thesis is to make a step towards solving this fundamental problem in computational materials science.

As a prestudy, we have selected Al, Cu and Rh and investigated their equation of state in two equivalent phases: in conventional face-centered-cubic lattice (fcc, str-I) and in a face-centered-cubic lattice with one atomic and three interstitial empty potential wells per primitive cell (str-II). We established the proper basis set of the exact muffin-tin orbitals as well as the proper potential sphere radius by calculating the equilibrium Wigner-Seitz radius and bulk modulus of the above elements in str-I and str-II using the exact muffin-tin orbitals (EMTO) first-principle density functional method. We have demonstrated that for Al *spd* orbitals are sufficient to describe the equilibrium bulk properties in both structures, while for str-II Rh and Cu at least five orbitals (*spdfg*) are needed to get accurate equilibrium volume and bulk modulus. Furthermore, we have shown that in general, for the str-II type of structure (close-packed structure with interstitials) the optimized overlapping muffin-tin potential in combination with *spdfg* orbitals ensures well converged bulk properties.

As an application of the above work in alloys, we studied (i) the chemical reaction between $ScAl_{1-x}Mg_x$ ($0 \leq x \leq 0.3$) random alloys and hydrogen H_2 molecule, (ii) the phase stability of the hydrogenated alloys in different structures and (iii) the hydrogen absorption/desorption temperatures by calculating the Gibbs energy for the components of the reaction. Experimental and theoretical studies by Sahlberg *et al.* showed that the $ScAl_{0.8}Mg_{0.2}$ compound with CsCl structure absorbs hydrogen by decomposing into ScH_2 with CaF_2 structure and fcc $Al_{0.8}Mg_{0.2}$. This reaction was found to be very fast, even without adding catalyst, and fully reversible. Our theoretical hydrogen absorption/desorption temperatures agree well with the experimental

values. On the other hand, we demonstrated that the stability field of the hydrogenated alloys strongly depends on the Mg content and on the microstructure of the hydrogenated alloys. For a given microstructure, the critical temperature for hydrogen absorption/desorption increases with the Mg concentration.

Steels are considered to be one of the most important engineering materials. They are mainly composed of iron and carbon. Other alloying elements in steel are introduced to get specific properties like microstructure, corrosion resistance, hardness, brittleness, etc. In order to describe the effect of carbon interstitial in iron alloys, it is important to know how the substitutional alloying elements affect the softness and some other properties of iron alloys. For that reason, we have investigated the alloying effects on the energetic and magnetic structure of paramagnetic $Fe_{0.85}Cr_{0.1}M_{0.05}$ (M = Cr, Mn, Fe, Co and Ni) alloys along the tetragonal distortion path connecting the body centered cubic (bcc) and the face centered cubic phases. It is shown that Cr stabilizes bcc phase and increases the energy barrier (relative to the bcc phase) between the fcc and bcc phases. Cobalt and Ni stabilize the fcc structure. Cobalt increases whereas Ni slightly decreases the energy barrier relative to the fcc structure. Manganese and iron have negligible effect on the structural energy difference as well as on the energy barrier along the Bain path. The local magnetic moments on Fe atoms have maximum values at bcc phase and minimum values at fcc phase. Cobalt atoms possess local magnetic moments only for tetragonal lattices with $c/a < 1.30$, and the Mn magnetic moments have almost constant value along the Bain path.

The electronic structure and total energy calculations from this thesis are based on the first-principles exact muffin-tin orbital method. The chemical and magnetic disorder was treated using coherent-potential approximation and the paramagnetic phase was modeled by the disordered local magnetic moments approach.

Acknowledgements

First Of all, all praise and thanks be to Allah, God the Almighty, Most Beneficent and Most Merciful.

There are lots of people I would like to thank for a huge variety of reasons. It is difficult to overstate my gratitude to my Ph.D. advisors, Professor Levente Vitos and Professor Börje Johansson for the opportunity to work in their group. Their enthusiasm for physics is both genuine and contagious. The perspective and approach they bring towards research have had a deep and beneficial influence on me. The inspiration of Professor Levente Vitos and his many efforts to explain things clearly and simply are highly appreciated. Thank you also for managing to read the whole thesis so thoroughly and for helpful comments on the text. Thanks for the many insightful conversations during the development of the ideas in this thesis.

Many thanks are also due my opponent, Prof. Liviu Chioncel, for having reviewed my thesis.

Colleagues and faculty members are thanked for numerous stimulating discussions and general advice; among others I would like to acknowledge Erna and Lorand for their help, especially concerning computer related problems. Marko thank you for fruitful collaboration. Thank you Chunmei, Hualei, Song Lu and Andreas.

For financial support, I thank the state of EMP JOSYLEEN (Erasmus Mundus Partnership JOrdan SYria LEbanon Europe Network) and Tafila Technical University for the scholarship award.

Finally, I am forever indebted to my family: my mother in law for long-distance cheerleading, my brothers and sisters were always heartening and encouraging, I am grateful to my dear parents who introduced me to science, taught me the value of hard work, and gave me endless support along the way, my husband Khalid for his understanding, endless patience and encouragement when it was most required and most of all for my son Hashem who makes my life full of joy and fun.

Stockholm, February 2011 Noura Al-Zoubi

List of included publications

I **Completeness of the exact muffin-tin orbitals: Application to hydrogenated alloys**

N. I. Al-Zoubi, M. P. J. Punkkinen, B. Johansson, and L. Vitos. *Phys. Rev. B* **81**, 045122 (2010).

II **Influence of Magnesium on hydrogenated $ScAl_{1-x}Mg_x$ alloys: a theoretical study**

N. Al-Zoubi, M. P. J. Punkkinen, B. Johansson and L. Vitos. Submitted to *Phys. Rev. B*

III **Bain Path of paramagnetic Fe-Cr based alloys**

N. Al-Zoubi, B. Johansson, G. Nilson and L. Vitos. Submitted to Acta Materialia

IV **Mechanical Properties and Magnetism: Stainless Steel Alloys from First-principles Theory**

L. Vitos, H. L. Zhang, N. Al-Zoubi, S. Lu, J. -O. Nilsson and B. Johansson. Submitted to Conference proceedings, MRS 2011 Fall Meeting

Comments on my own contribution

Paper I: design research 20%, perform calculations 80%, analyze results 50%, and prepare the manuscript 60%.

Paper II: design research 20%, perform calculations 80%, analyze results 70%, and prepare the manuscript 70%.

Paper III: design research 20%, perform calculations 100%, analyze results 70%, and prepare the manuscript 70%.

Paper IV: perform calculations 10%.

Contents

Chapter 1

1. Introduction

1.1 Introduction to Defects

Even though crystals are defined as ordered arrangements of atoms or ions, they are not perfect. There always exist crystalline defects, which can be point defects occurring at a single lattice point; line defects occurring along a row of atoms; or planar defects occurring over a two-dimensional surface in the crystal. There can also be three-dimensional defects such as voids [1]. Defects influence the electrical and mechanical properties of solids; in fact it is the defects that are usually responsible for the existence of useful properties. Almost, or perhaps all, technologically relevant materials depend on the existence of some kind of defects. An interstitial impurity is defined as a point defect atom occupying the space between regular lattice sites. Figure 1.1 shows a schematic plot of the two most common interstitials. Interstitials have wide applications such as they are used for storage of hydrogen in metals [2, 3], interstitial carbon atoms are used in steels to get useful properties [4], interstitial are important for starting glass transition [5-7].

In the present thesis we select Al, Cu and Rh and try to describe them in the original fcc lattice and in an fcc lattice with interstitial sites. In order to make these "interstitials" very anisotropic we fill them with empty potential wells. That is, physically the original fcc lattice and the fcc lattice with interstitial are completely equivalent. However, from computational point of view the latter case represents a great challenge due to the low symmetry, large overlap between atomic and interstitial sites and loosely packed lattice sites. Our goal is to find a proper numerical approach which yields the same ground state properties for the "dressed up" fcc lattice as those obtained for the parent fcc lattice. In this test we monitor the electronic structure, equilibrium volume and bulk modulus. The reason for performing the test with a muffin-tin approach is that in contrast to most of the full-potential approaches, the presently employed density functional tool can handle disordered systems as well. Therefore, after having established a proper numerical approach, one can go further and insert true interstitials in the close-packed metals and alloys and study their impact on the basic properties.

As an application of our methodological developments, we considered a very important field, namely the problem of hydrogen storage in solids. The field is briefly introduced in Section 1.2. We focused on the *ab* initio description of the properties of the $ScAl_{1-x}Mg_x$ hydrogenated alloys as a function of Mg content, microstructure, and external conditions (temperature and pressure).

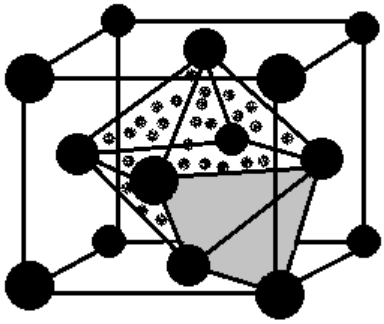

Figure 1.1 *Octahedral* (dotted area) and *tetrahedral* (shaded area) interstitial in a face-centered cubic lattice.

1.2 Hydrogen Storage in Metals

Hydrogen is the ideal candidate as an energy carrier for both mobile and stationary applications while averting adverse effects on the environment. Hydrogen storage is clearly one of the key challenges in developing hydrogen economy.

Hydrogen can be stored as (i) pressurized gas, (ii) cryogenic liquid, (iii) solid fuel as chemical or physical combination with materials, such as metal hydrides, complex hydrides and carbon materials. Each of these options possesses attractive attributes for hydrogen storage [8, 9]. Liquid hydrogen requires the addition of a refrigeration unit to maintain a cryogenic state [10] thus adding weight and energy costs, and a resultant 40% loss in energy content [11]. High-pressure storage of hydrogen gas is limited by the weight of the storage canisters and the potential for developing leaks. Moreover, storage of hydrogen in liquid or gaseous form poses important safety problems for on-board transport applications. Hydrogen forms metal hydrides with some metals and alloys leading to solid-state storage under moderate temperature and pressure that gives them the important safety advantage over the gas and liquid storage methods. Metal hydrides have higher hydrogen-storage density than hydrogen gas or liquid hydrogen. Hence, metal hydride storage is a safe, volume-efficient storage method for on-board vehicle applications.

Light metals form a large variety of metal-hydrogen compounds [12-15]. They are especially interesting due to their light weight and the number of hydrogen atoms per metal atoms, which is often of the order of 2. Most of the hydrogen absorption investigations are based on experimental studies. In this thesis we present a systematic theoretical study of the effect of Mg on the phase stability of the hydrogenated $ScAl_{1-x}Mg_x$ $(0 \leq x \leq 0.3)$ random alloys using the exact muffin-tin orbital method in combination with the coherent potential approximation. In order to establish the accuracy of our method (EMTO) we used the projector augmented wave (PAW) method to describe hydrogenated (ScAl) alloys.

1.3 The fcc-bcc Bain Path Deformation

Carbon and nitrogen are frequently used in steels. They occupy interstitial positions and are primarily responsible for the formation of martensites. Describing their impact on the basic properties is a fundamental question in computational steel science. As a first step in this challenging task, we studied the deformation path between the competing cubic phases as a function of substitutional alloying elements.

Homogeneous transformation describes a continuous crystallographic transition from initial to final phase. For bcc-fcc martensitic transformation a few homogeneous strain paths have been developed [16-18]. The simplest one is known as the Bain deformation [19]. This path consists of a continuous expansion of a bcc lattice along one of the cubic axes (*c*) with a contraction along the two others (*a*). When the *c/a* ratio reaches $\sqrt{2}$, the body-centered-tetragonal lattice (bct) becomes fcc as shown in figure 1.2. The Bain path is unique in that it retains the highest possible (tetragonal) crystal symmetry. The Bain path is a convenient tool for investigating the energetics of the bcc-fcc transformation.

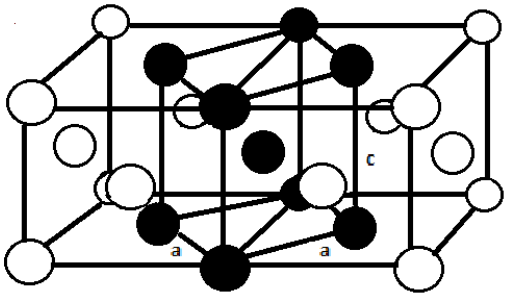

Figure 1.2 Schematic of the body centered tetragonal (bct) unit cell (in black) which allows a continuous (Bain) transformation between bcc ($c/a = 1$) and fcc ($c/a = \sqrt{2}$) lattices.

We present calculations about the total energy, the softness of fcc and bcc lattices and the local magnetic moments of the paramagnetic Fe-Cr-M (M = Cr, Mn, Co, Ni) alloys along the Bain path as a function of *c/a* ratio and Wigner-Seitz radius (*w*). We consider this work as basis for our future work on carbon steel.

Chapter 2

2. First Principle Calculations

A large number of material properties can be understood by the electronic structure. We can find these properties either by semi-empirically or from first principles quantum theory. Describing the properties of materials from first principles theory implies solving the Schrödinger equations for a huge number of interacting electrons and nuclei. Many programs have been developed for first principles calculations based on density functional theory. In this chapter the Schrödinger equation, the density functional theory and some common approximations within it, and the exact muffin-tin orbitals method are briefly reviewed.

2.1 Schrödinger Equation

For a non-relativistic quantum system, consisting of *N* electrons and *M* nuclei, we use the time independent Schrödinger equation [20]

$$H\psi(\vec{r_1},....,\vec{r_N},\vec{R_1},\dots,\vec{R_M}) = E\psi(\vec{r_1},....,\vec{r_N},\vec{R_1},\dots,\vec{R_M}), \quad 2.1$$

where ψ is the wave function, an eigenstate of the Hamiltonian *H*.

$$\widehat{H} = -\frac{\hbar^2}{2m_e}\sum_i^N \nabla_{r_i}^2 - \frac{\hbar^2}{2M_I}\sum_I^M \nabla_{R_I}^2 - \sum_{i,I}^{N,M}\frac{Z_I e^2}{|\vec{r}_i-\vec{R}_I|} + \frac{1}{2}\sum_{i\neq j}^{N,N}\frac{e^2}{|\vec{r}_i-\vec{r}_j|} + \sum_{I\neq J}^{M,M}\frac{Z_I Z_J e^2}{|\vec{R}_I-\vec{R}_J|}. \quad 2.2$$

M denote the mass of an ion, R is the nuclear position vector and Z is the charge of an ion. m denote the electron mass, r is the electronic position and e is the electron charge. $\hbar$ is Planck constant. The first and second term in Equation 2.2 are the kinetic energy operators for electrons and nuclei, the third, fourth and fifth terms are the potential operators that describe electron-nucleus, electron-electron and nucleus-nucleus interactions.

Solving the above Schrödinger equation is an impossible task even for relatively small systems. The first step to overcome this objection is given by Born-Oppenheimer approximation [21]. It assumes that due to the large difference in mass between electrons and nuclei, the nuclei will move so slowly that the electrons will remain in their given states as the nuclei move and we

may now treat the electrons as if they were moving in an environment of static nuclei, and the Schrödinger equation can be reduced to

$$\left(-\frac{\hbar^2}{2m_e}\sum_i^N \nabla_{r_i}^2 - \sum_{i,I}^{N,M}\frac{Z_i e^2}{|\vec{r}_i-\vec{R}_I|} + \frac{1}{2}\sum_{i\neq j}^{N,N}\frac{e^2}{|\vec{r}_i-\vec{r}_j|}\right)\psi = (T + V_{ext} + V_H)\psi = E\,\psi. \qquad 2.3$$

Here T is the electronic kinetic energy, V_{ext} is the external Coulomb potential from the interactions between electrons and nuclei, and V_H is Hartree potential i.e. the Coulomb potential from the interactions between the electrons.

The above reduced Schrödinger equation describing the electrons is still too complex for practical purposes. Other approximations are still needed. *Density functional theory* offers an elegant reformulation of this problem. In the next subsection this theory is outlined.

2.2 Density Functional Theory

Density functional theory (DFT) is based on two main theorems described in the paper by Hohenberg and Kohn [22]: the first theorem says that the ground state electron density $n(\vec{r})$ determines the potential of a system; we may conclude that all ground states properties of a system are completely determined by the ground state density. This emphasizes the importance of the electron density within the DFT, and the solution of the Schrödinger equation becomes less cumbersome since the explicit use of the many-body wave function is no longer needed. The second theorem comprises a variational principle for the total energy and states that the minimum of the energy functional is the ground state energy. The ground state electron density and the total energy are calculated within the formulation of Kohn and Sham [23], which assumes that the density of a system of interacting electrons can be obtained as the density of an auxiliary system of non-interacting particles, moving in an effective potential. Within the Kohn-Sham scheme, the variational principle leads to the effective single-electron Schrödinger equations

$$-\nabla^2 + v([n];r)\}\,\psi_j(r) = \epsilon_j\,\psi_j(r), \qquad 2.4$$

where v is the effective potential. The non-interacting Kohn-Sham system is subject to an effective potential

$$v([n];r) = v_e\,(r) + v_H([n];r) + \mu_{xc}([n];r). \qquad 2.5$$

Here the second term is the Hartree potential,

$$v_H([n];r) = 2\int \frac{n(r')}{|r-r'|}\,dr'. \qquad 2.6$$

For electrons moving in the external potential created by the fixed nuclei located on lattice sites **R** we have

$$v_e(r) = -\sum_R \frac{2Z_R}{|r-R|} \qquad 2.7$$

and the last term is the exchange-correlation potential defined as the functional derivative of $E_{xc}[n]$, i.e.

$$\mu_{xc}([n];r) = \frac{\delta E_{xc}[n]}{\delta n(r)}. \qquad 2.8$$

This term includes the exchange energy due to Pauli Exclusion Principle and all the interactions between particles that are not included in the above terms. The ground state density for an N electron system is given by single electron wave functions

$$n(r) = \sum_{i=1}^{N} |\psi_i(r)|^2. \qquad 2.9$$

In this expression, the summation runs over all the Kohn-Sham states below the Fermi level ε_F, which in turn is obtained from the condition

$$N_e = \int n(r)dr, \qquad 2.10$$

where N_e is the number of electrons. The self-consistent solution of the above equations is used to compute the ground state energy of the electronic system

$$E_e[n] = T_s\,[n] + \frac{1}{2}\int v_H([n];r)\,n(r)dr + E_{xc}[n] + \int v_e\,(r)n(r)dr. \qquad 2.11$$

Then the total energy of the system formed by electrons and nuclei is just the summation of equation 2.11 and nuclear-nuclear repulsion, viz.

$$E_{tot} = E_e[n] + \sum_{RR'} \frac{Z_R Z_{R'}}{|R-R'|}. \qquad 2.12$$

For a spin-polarized system, the density is divided into two spin densities $n^{\uparrow}(r)$ and $n^{\downarrow}(r)$. They are solutions of the Kohn-Sham equation for the spin-dependent effective potential. The remaining unknown term is the exchange-correlation term. This energy term cannot be evaluated exactly but it plays an important role in defining the physics of the system. Therefore much effort has been put into approximating the exchange-correlation term.

2.2.1 The Exchange-Correlation Energy

The exchange interaction is due to Pauli Exclusion Principle [1], while correlation term includes all interactions which are not explicitly included in the kinetic energy, Hartree and exchange terms. The simplest approximation for the exchange-correlation energy within DFT is the local density approximation (LDA) [24, 25]. Within the LDA, the exchange-correlation energy is assumed to be the same as that in a homogenous electron gas,

$$E_{XC}^{LDA}[n] = \int d^3r n(r)\varepsilon_{XC}^{hom}(n(r)), \qquad 2.13$$

where $\varepsilon_{XC}^{hom}(n(r))$ is the sum of the exchange and correlation energies of the homogeneous electron gas of density $n(r)$. The LDA approach is based on the homogeneous electron gas, therefore it is less accurate for systems where the density varies rapidly. Improvement over LDA has led to generalized gradient approximation (GGA) of the exchange-correlation functional. This alternative provides non-local information of the density using the gradient of the electron density. A general expression of the GGA is

$$E_{XC}^{GGA}[n] = \int d^3r n(r)\varepsilon_{XC}^{hom}[n; |\nabla n|). \qquad 2.14$$

There are several functional forms for GGA, the most common versions of the GGA implemented in DFT computational programs are: The one developed by Perdew, Burke and Ernzerhof (PBE) [26] and later revised for solids and surfaces (PBE_{sol}) [27]. The PBE works better than the LDA for bulk properties of simple and 3*d* transition metals. Therefore, in this thesis, the GGA-PBE has been used for the exchange-correlation functional to describe the properties of 3*d* metals and metallic alloys.

2.3 Computational Tools

Many different *ab initio* methods have been developed to solve the Kohn-Sham equations. The required accuracy for the Kohn-Sham method is always set by the actual property to be computed. For instance, an approximate solution of the Kohn-Sham equations can provide useful information about properties calculated for a fixed crystal structure, whereas quantities involving lattice distortions or structural energy differences require a high level of accuracy. Because of this, often a compromise has been made between accuracy and efficiency, and methods employing certain approximations have been developed. In this thesis implementations and applications of the exact muffin-tin orbital (EMTO) method combined with the coherent-potential approximation and the full charge density technique are discussed. The projector augmented wave (PAW) method was used in order to assess the accuracy of the EMTO, and therefore it is not discussed here.

2.3.1 Exact Muffin-tin Orbital Method

An important group of density-functional methods is built around the so-called muffin-tin (MT) approximation. The approximation originates from the observation that the exact crystal potential is atomic like around the lattice sites, where the core states are located, and nearly flat between the atoms. Accordingly, within the MT approximation one substitutes the Kohn-Sham effective potential by spherically symmetric potentials centered on atoms plus a constant potential in the interstitial region. The MT family includes the standard Korringa-Kohn-Rostoker (KKR) [28, 29] and screened-KKR [30] methods, methods based on the atomic sphere approximation (ASA) [31-34] as well as the recently developed exact muffin-tin orbital method by Andersen and co-worker [35] and implemented by Vitos [36-39]. The EMTO method is an improved screened Korringa-Kohn-Rostoker method, in that large overlapping potential spheres can be used for an accurate representation of the exact single electron potential. The single-electron states are calculated exactly, while the potential can include certain shape approximations, if required. Within the overlapping muffin-tin approximation, the effective single-electron potential in Equation 2.5 is approximated by spherical potential wells $v_R(r_R) - v_0$ centered on lattice sites R plus a constant potential $v_0, viz.$

$$v(r) \approx v_{mt}(r) \equiv v_0 + \sum_R [\, v_R(r_R) - v_0], \qquad 2.15$$

$v_R(r_R)$ becomes equal to v_0 outside the potential sphere of radius s_R. For fixed potential spheres, the spherical and the constant potentials are determined by optimizing the mean of the squared deviation between $v_{mt}(r)$ and $v(r)$, $i.e.$ minimizing the functional

$$F_v[\{v_R\}, v_0] \equiv \int\{v(r) - v_0 - \sum_R[v_R(r_R) - v_0]\}^2 dr. \quad 2.16$$

The integral is performed over the entire unit cell. Since the F_v is a functional of the spherical potentials, the minimum condition is expressed as

$$\int \delta v_R(r) \frac{\delta F_v[\{v_R\}, v_0]}{\delta v_R(r)} dr = 0 \quad \text{for any } R, \quad 2.17$$

where $\delta/\delta v_R(r)$ stands for the functional derivative, and

$$\frac{\delta F_v[\{v_R\}, v_0]}{\delta v_R(r)} = 0. \quad 2.18$$

The solution of these integro-differential equations gives the optimal $v_R(r_R)$ and v_0, and leads to the so called *optimized overlapping muffin-tin* (OOMT) potential.

2.3.1.1 Exact Muffin-tin Orbitals Wave Functions

We solve the single-electron Equation 2.4 for the muffin-tin potential defined in Equation 2.15, by expanding the Kohn-Sham orbital $\psi_j(r)$ in terms of the *exact muffin-tin orbitals* $\bar{\psi}^a_{RL}(\epsilon_j, r_R)$, $viz.$

$$\psi_j(r) = \sum_{RL} \bar{\psi}^a_{RL}(\epsilon_j, r_R)\, v^{\mathrm{a}}_{RL,j}. \quad 2.19$$

The expansion coefficients, $v^{\mathrm{a}}_{RL,j}$, are determined from the condition that the above expansion should be solution of Equation 2.4 in the entire space. In the EMTO formalism, the algebraic formulation of this matching condition is the so called kink cancellation equation [36, 39-40]. The exact muffin-tin orbitals are constructed using different basis functions inside the potential spheres and in the interstitial region. In the interstitial region, where the potential is approximated by v_0 the basis functions are solutions to the free electron Schrödinger equation. The boundary conditions for the free electron Schrödinger equation are given in conjunction with non-overlapping spheres, called *hard spheres* centered at lattice site R and with radius a_R. These functions are called *screened spherical waves* [36]. The screened spherical waves are defined as

being free electron solutions which behave as real harmonics on their own a-spheres centered at site R and vanish on all the other sites. Inside the potential sphere the basis functions are called *partial waves*, they are defined as the products of the regular solutions of the radial Schrödinger equation [41] for the spherical potential and the real harmonics. Because screened spherical wave behaves like real harmonic only on its own a-sphere, the matching condition between the two basis functions should be set up at this sphere. On the other hand, and as we know for an accurate representation of the single-electron potential the potential spheres should overlap. Therefore, usually we have $s_R > a_R$. Because of this, an additional free-electron solution has to be introduced. This function realizes the connection between the screened spherical wave at a_R and the partial wave at s_R. It joins continuously and differentiable to the partial wave at s_R and continuously to the screened spherical wave at a_R. Finally, the exact muffin-tin orbitals are constructed as the superposition of the screened spherical waves, the partial waves and the free-electron solution. In the present method the Green's function formalism is employed. Both self-consistent single electron energies and the electron density can be determined within Green's function formalism.

2.3.1.2 The Full Charge Density (FCD) Technique

The *Full Charge Density* (FCD) [42-44] technique is designed to maintain high efficiency but at the same time to give total energies with an accuracy similar to that of the full-potential methods. The principal idea behind the FCD technique is to use the total charge density to compute the total energy functional given by Equation 2.11. The total density can be taken from a self-consistent calculation employing certain approximations. In the present case we use the EMTO total charge density which is given by

$$n(r) = \sum_R n_R(r_R) \qquad 2.20$$

Here we divide the total density $n(r)$ into components $n_R(r_R)$ defined inside the Wigner-Seitz cells [45]. Around each lattice site we expand the density components in terms of the real harmonics, *viz*.

$$n_R(r_R) = \sum_L n_{RL}(r_R) Y_L(\hat{r}_R) \qquad 2.21$$

In order to be able to compute the energy components from Equation 2.11 we need to establish technique to calculate the space integrals over the Wigner-Seitz cells. For this we adopt the *shape function technique* [46]. Within the shape function any integral over the cell can be transformed into an integral over the sphere which circumscribes the cell. The shape function is a 3D step function defined as 1 inside the Wigner-Seitz cell and zero otherwise. By combining the FCD and the shape function technique the total energy can be calculated by dividing it into the kinetic energy, the exchange-correlation energy and the electrostatic energy. The latter is divided into the intra-cell and inter-cell contributions. Then, the total energy becomes

$$E_{tot} = T_s[n] + \sum_R (F_{intraR}[n_R] + E_{xcR}[n_R]) + F_{inter}[n] \qquad 2.22$$

Where the intra-cell $F_{intraR}[n_R]$ and the exchange-correlation energies $E_{xcR}[n_R]$ depend only on the charge density within the actual cell, whereas $F_{inter}[n]$ depends on the charge distributions around different cells and T_s is a nonlocal functional of the density. These terms are accurately calculated within the FCD technique.

2.3.1.3 Coherent Potential Approximation (CPA)

The most powerful technique in the case of disordered alloys is the *Coherent Potential approximation* (CPA). The CPA was introduced by Soven [47] for the electronic structure problem and by Taylor [48] for phonons in random alloys. Györffy [49] formulated the CPA using the Green function technique. The CPA is based on the assumption that the alloy may be replaced by an ordered effective medium. The impurity problem is treated within the *single-site* approximation. This means that one single impurity is placed in an effective medium and no information is provided about the individual potential and charge density beyond the sphere around this impurity. Within the EMTO method we construct the CPA effective medium by calculating the Green functions of the alloy components. We can calculate the Green functions by substituting the coherent potential of the CPA medium by the real atomic potentials and the average of the individual Green functions should reproduce the single-site part of the coherent Green function. These are solved iteratively and the output is used to determine the electronic structure, charge density and total energy of the random alloy.

Chapter 3

3. Interstitials in Metals and Alloys

In the sections below a series of calculations and analyses on metals and alloys by using the EMTO method are described. First, the equilibrium bulk properties of Al, Cu and Rh in fcc lattice and in an fcc lattice with empty interstitial sites are examined. Then the phase stability field of the hydrogenated Sc-Al-Mg alloys are investigated in details.

3.1 Basis Set Convergence of the Exact Muffin-tin Orbitals

We have investigated the basis set convergence of the exact muffin-tin orbitals by monitoring the equation of state for Al, Cu and Rh calculated in the conventional fcc lattice (str-I). Then, we insert three empty interstitial sites per fcc primitive cell: one to the (½, ½, ½) octahedral position and two to the (¼, ¼, ¼) and (¾, ¾, ¾) tetrahedral positions (str-II). The resulting lattice has a body-centered-cubic (bcc) packing and can be used as a prototype for large variety of systems. We select Al, Cu and Rh as three representative fcc metals having markedly different electronic structures and charge densities. In order to monitor the performance of the muffin-tin approach for structures str-I and str-II, we choose two fundamental quantities: the equilibrium Wigner-Seitz radius (w) and the bulk modulus (B). On the other hand, we have treated the radii of the potential spheres (S) for str-II as variables. Therefore, by employing EMTO method in the present work, in addition to the basis set, we have investigated how the size of the overlapping MT potential spheres influences the accuracy of the calculated physical properties.

3.1.1 Structure str-I

Theoretical equilibrium Wigner-Seitz radii and bulk moduli for fcc (str-I) Al, Cu and Rh are listed in Table I as function of number of muffin-tin orbitals, l_{max} for PBE-GGA exchange-correlation functional. In order to test the accuracy of the calculations, the theoretical w and B are compared with the experimental values taken at room temperature [50].

Table 3.1 Calculated equilibrium atomic radii (w in bohr) and bulk moduli (B in GPa) for fcc Al, Cu, and Rh as functions of the number of MT orbitals, l_{max} compared with experimental values [50]. Results are shown for PBE exchange-correlation approximation.

	w					B				
	spd	*spdf*	*spdfg*	*spdfgh*	*Exp*	*spd*	*spdf*	*spdfg*	*spdfgh*	*Exp*
Al	2.99	2.99	2.99	2.99	2.991	75.1	75.7	75.7	75.7	72.8
Cu	2.70	2.69	2.68	2.68	2.669	135.5	140.5	141.5	141.6	133
Rh	2.88	2.84	2.83	2.83	2.803	235.4	252.4	255.5	255.9	282

Taking the most accurate values those corresponding to *spdfgh*, from Table 3.1 we can establish the basis set convergence for str-I. For fcc Al already $l_{max} = 2$ leads to well-converged w and B, whereas for fcc Cu and Rh $l_{max} = 3$ is required to reduce the errors of w and B to 0.4% and 1.4%,

3.2.1 Structure str-II

Figure 3.1 shows the relative errors for the w (δ_w) and B (δ_B) of Al calculated for str-II as a function of l_{max} and S. Here the errors are defined as the relative deviations between w of str-II and $w = 2.95$ Bohr of str-I using *spdfgh* and LDA approximation and between B of str-II and $B = 81.2$ GPa of str-I using *spdfgh* and LDA approximation. The relative errors for str-I are also shown as a function of l_{max}.

We find that for Al there are no significant differences between the errors and their l_{max} dependence obtained for both structures. For all S values w and B converged rapidly with l_{max}, we ascribe this good convergence to the well-localized core density and the nearly homogeneous valence density in this metal. No improvement is achieved by increasing the potential radius to $1.05w$ and $1.10w$.

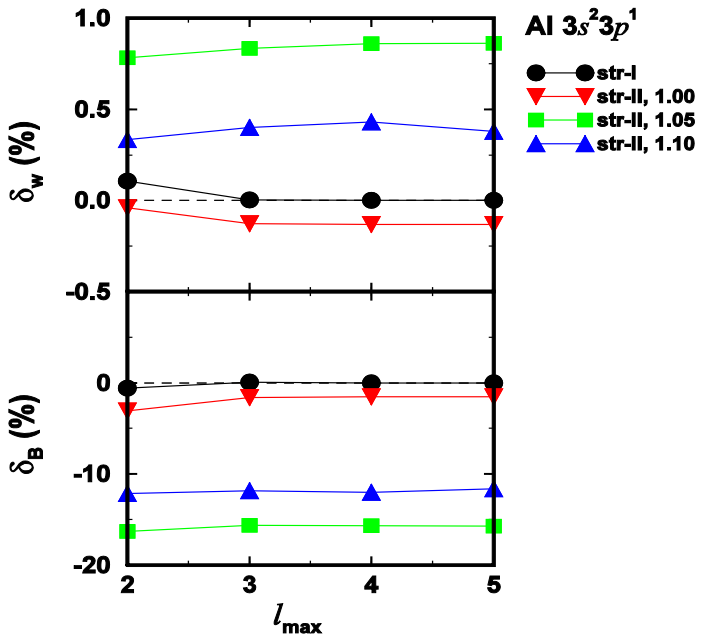

Figure 3.1 Relative errors of the LDA equilibrium WS radius and bulk modulus for Al calculated for str-II structure as functions of the number of MT orbitals l_{max} and potential sphere radius (S = 1.00w, 1.05w and 1.10w). Solid circles describe the error obtained for str-I Al.

The fcc Cu shows converged results at l_{max} = 3, while for str-II Cu at least l_{max} = 4 (*spdfg*) is needed to stabilize δ_w and δ_B . Concerning the potential sphere dependence of δ_w and δ_B we found that S = 1.05w yields accurate volume for *spdfg* and *spdfgh* ($|\delta_w| < 0.3\%$). However, this choice of S produces large error in the bulk modulus of Cu ($|\delta_B| \approx 17\%$). By increasing the S = 1.10w the error decreases to 0.1% but increases $|\delta_w|$ to 2.21%. We explain the relatively large error for str-II Cu by the semi-core states, which may give a non-spherical charge distribution around tetrahedral sites, therefore we did additional calculations for str-II Cu by including 3p semi-core states into valence states (referred to as Cu*). Figure 3.2 shows the results of str-II Cu (solid lines) and Cu*(dashed lines) as a function of l_{max} compared to the values of str-I Cu (solid lines). We observed that by placing the 3p states into the valence the relative error for the Wigner-Seitz radius decreases by ~ 2% and the bulk modulus of the two set of data agree quite well with each other.

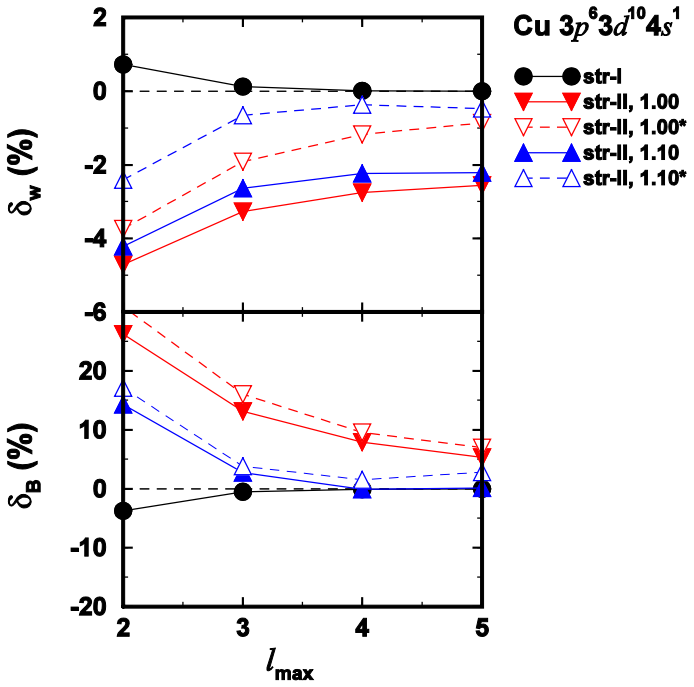

Figure 3.2 Relative errors of the LDA equilibrium WS radius and bulk modulus for Cu calculated for str-II structure as functions of the number of MT orbitals l_{max} and potential sphere radius (S = 1.00w, and 1.10w). Solid lines are the errors obtained for str-I and str-II Cu, dashed lines are the errors obtained for str-II Cu* (valence states are $3p^6 3d^{10} 4s^1$).

The basis set convergence for Rh in str-II structure is slower compared to that for Cu. The relative errors of Wigner-Seitz radius (δ_w) and bulk modulus (δ_B) are listed in Table 3.2. In general the two transition metals require a larger basis set than Al. To explain this trend, we compare the charge distributions in Rh and Cu. Fcc Rh has a larger interstitial charge density compared to Cu. According to our atomic calculations, in Rh approximately 0.13 electrons (~ 2% of the 4p electrons) are located outside of the sphere of radius w. In the case of Cu ~ 99% of the 3p electrons and for Al all 2p electrons are constrained within their Wigner-Seitz sphere. Thus, there is a strongly inhomogeneous charge density around the tetrahedral Em sites in str-II Rh, which explains the slow basis convergence of this system. The best results for the potential sphere dependence of str-II Rh is found for S = 1.10w, where the relative errors are the smallest for $l_{max} \geq 4$.

Table 3.2 Relative errors (in %) of the LDA equilibrium Wigner-Seitz radius (δ_w) and bulk modulus (δ_B) for Rh ($4p^6 4d^7 5s^2$) calculated for str-II as functions of l_{max} and *S*. The errors are relative to w = 2.78 Bohr and B = 313.9 GPa obtained for str-I structure using *spdfgh* basis.

	δ_w			δ_B		
S	*spdf*	*spdfg*	*spdfgh*	*spdf*	*spdfg*	*spdfgh*
1.00	-1.96	-1.10	-0.79	12.5	3.9	0.6
1.05	2.53	3.33	3.48	-25.7	-22.9	-23.2
1.10	-0.33	0.04	-0.06	-0.4	-3.5	-2.6

3.2 Application to Hydrogenated Alloys

3.2.1 The Chemical Reaction

In this work we have studied the reaction between $ScAl_{1-x}Mg_x$ having the CsCl structure and the H_2 gas, *viz*,

$$0.5ScAl_{1-x}Mg_x + 0.5x'H_2 \rightarrow Sc_{0.5}Al_{(1-x)/2}Mg_{x/2}H_{x'}, \quad 3.1$$

where $0 \leq x \leq 0.3$ and $0 \leq x' \leq 2$. The Gibbs energy of formation for the above reaction is

$$\Delta G\left(T, x', x, p_{H_2}\right) = \Delta G'(T, x', x) - \Delta G''\left(T, x', x, p_{H_2}\right). \quad 3.2$$

The reaction becomes exothermic when $\Delta G'(T, x', x) < \Delta G''\left(T, x', x, p_{H_2}\right)$. $\Delta G'$ is defined as the Gibbs energy of formation of the hydrogenated $Sc_{0.5}Al_{(1-x)/2}Mg_{x/2}H_{x'}$ alloy relative to the random H-rich and H-free alloys in the CaF_2 structure and is given by

$$\Delta G'(T, x', x) \equiv G'(T, x', x) - 0.5x'G_2(T, x) - (1 - 0.5x')G'_0(T, x), \quad 3.3$$

where $G_2(T, x)$ and $G'_0(T, x)$ are the Gibbs energies of $Sc_{0.5}Al_{(1-x)/2}Mg_{x/2}H_2$ and $Sc_{0.5}Al_{(1-x)/2}Mg_{x/2}$, respectively. The Gibbs energy of the reactant is given by

$$\Delta G''\left(T, x', x, p_{\mathrm{H}_2}\right) = \frac{1}{2}x'\left[G_{\mathrm{H}_2}\left(T, p_{\mathrm{H}_2}\right) - G_2(T,x) + G'_0(T,x)\right] + [G_0(T,x) - G'_0(T,x)]. \quad 3.4$$

The first term of the right hand side of Equation 3.4 represents the binding energy difference of H atoms in the H_2 molecule and in $Sc_{0.5}Al_{(1-x)/2}Mg_{x/2}H_2$ having the CaF_2 structure. The last term is the difference between the Gibbs energy of disordered $Sc_{0.5}Al_{(1-x)/2}Mg_{x/2}$ in the fcc structure $G'_0(T,x)$ and that of partially ordered $ScAl_{1-x}Mg_x$ in the CsCl structure $G_0(T,x)$. Here we assume that for the present solids the main temperature effect in the Gibbs energy is represented by the configurational entropy, since all solids possess similar Debye temperatures [51], the phonon contributions are estimated to be negligible compared to the entropy terms in $G_{\mathrm{H}_2}\left(T, p_{\mathrm{H}_2}\right)$.

The Gibbs energy of the hydrogen reservoir is [52]

$$G_{H_2}\left(T, p_{\mathrm{H}_2}\right) = E_{\mathrm{H}_2} + k_B T\left[ln\left(\frac{p_{\mathrm{H}_2}}{k_B T n_Q}\right) - lnZ_{int}\right] \quad 3.5$$

Where $n_Q = (mk_BT/2\pi\hbar^2)^{3/2}$ is the quantum concentration (m stands for the mass of a H_2 molecule, $\hbar$ is the Planck constant, k_B is the Boltzmann constant), and Z_{int} is the partition function of the internal states due to the rotational and vibrational degrees of freedom. We used the theoretical value (generalized gradient level) for the total energy of H_2 molecule $E_{\mathrm{H}_2} = -2.345\ Ry$ [53]. We used the numerical parameters for H_2 from [54, 55].

For the hydrogenated alloys $Sc_{0.5}Al_{(1-x)/2}Mg_{x/2}H_{x'}$ having the CaF_2 parent lattice we used several different structures. First, for arbitrary hydrogen contents we assumed that the Ca sublattice is occupied entirely by the $Sc_{0.5}Al_{(1-x)/2}Mg_{x/2}$ random alloys and the F sublattice by $H_{x'}$ plus empty potential wells. Second for 50% hydrogen content (i.e $x' = 1$) we considered two structures. The first model is a completely phase separated system (PS) represented by bulk ScH_2 plus bulk $Al_{1-x}Mg_x$. The Gibbs energy per metal atom for this structure is

$$G^{PS} = [G(ScH_2) + G(Al_{1-x}Mg_x)]/2\ . \quad 3.6$$

The second model is a composite similar to PS but with finite grain sizes (PSi). In this model we assume that the ScH_2 grains embedded in $Al_{1-x}Mg_x$ matrix have a cubic shape with edges equal to $\lambda \approx na$ (a is the average lattice constant). Within this approach the Gibbs energy of formation

for the composite can be written as $\Delta G(\lambda) = \lambda^3 \Delta g + 6\lambda^2 \gamma_i$, where γ_i stands for interfacial energy expressed per unit area and Δg is the Gibbs energy density gain associated with the phase separation. The extremum of $\Delta G(\lambda)$ determines the minimum grain size $\lambda_{min} \approx 4\gamma_i/\Delta g$, below which no phase separation occurs. Then, the Gibbs energy per metal atom for PSi can be written in the form

$$G^{PSi}(n) \approx \frac{1}{2}[G(\mathrm{ScH_2}) + G(\mathrm{Al_{1-x}Mg_x})] + \frac{3a^2}{4n}\gamma_i, \qquad 3.7$$

where n is the size of finite grain. When γ_i is negligible or when the size of the grains is very large ($n \gg 1$), $G^{PSi}(n)$ reduces to G^{PS}. In order to compute the interfacial energy between ScH_2 and $\mathrm{Al_{1-x}Mg_x}$ grains, we did the total energy calculation for two layered structures. The first structure we denoted by LS has a unit cell formed by two adjacent fcc cells. The first fcc cell is filled up with $\mathrm{ScH_2}$ having the $\mathrm{CaF_2}$ structure and the second with $\mathrm{Al_{1-x}Mg_x}$ having the fcc structure. The second structure is a double layered structure denoted by LS2 formed by four adjacent cubic fcc unit cells (two $\mathrm{CaF_2}$ $\mathrm{ScH_2}$ cells and two fcc $\mathrm{Al_{1-x}Mg_x}$ cells). By using these structures we calculated the interfacial energy as

$$\gamma_i = \frac{E^{LS} - 4E^{incr}}{2A_i}, \qquad 3.8$$

where the incremental energy is the bulk energy ($E^{incr} = (E^{LS2} - E^{LS})/4$) and $A_i = a^2/2$ is the interface area per metal atom.

3.2.2 Effect of Mg Addition and Microstructure on the Stability of the Hydrogenated $\mathbf{ScAl_{1-x}Mg_x}$ Alloys

According to our calculations we observed that $\Delta G''\left(T, x', x, p_{\mathrm{H_2}}\right)$ term exhibits much stronger temperature dependence than the $\Delta G'(T, x', x)$ term. This strong temperature dependence of $\Delta G''$term in turn is due to the entropy of the hydrogen reservoir (Equation. (3.5)).

We found that the hydrogenation reaction for the random solid solution $\mathrm{Sc_{0.5}Al_{(1-x)/2}Mg_{x/2}H_{x'}}$ in $\mathrm{CaF_2}$ structure is always endothermic, i.e. the hydrogenated alloys is unstable for all $x', T, p_{\mathrm{H_2}}$ considered here. Our calculations show that $\Delta G'(T, 2, x) - \Delta G''\left(T, 2, x, p_{\mathrm{H_2}}\right)$ decreases substantially with Mg addition. For instance, at 0 K the above Gibbs energy difference changes

from 14 mRy at $x = 0$ to 6.4 mRy at $x = 0.2$. On the other hand, the above energy difference increases with increasing the temperature from 0 K to 800 K at 100 kPa, and at 10 MPa. At $x = 0.2$ and $x' = 2$, the above energy difference increases from 14.31 mRy at 0 K to 90.1 mRy (66.7 mRy) at 800 K and 100 kPa (10 MPa) (see Figure 3.4). Pressure destabilizes the quasi-ordered CsCl structure as shown in Figure 3.3

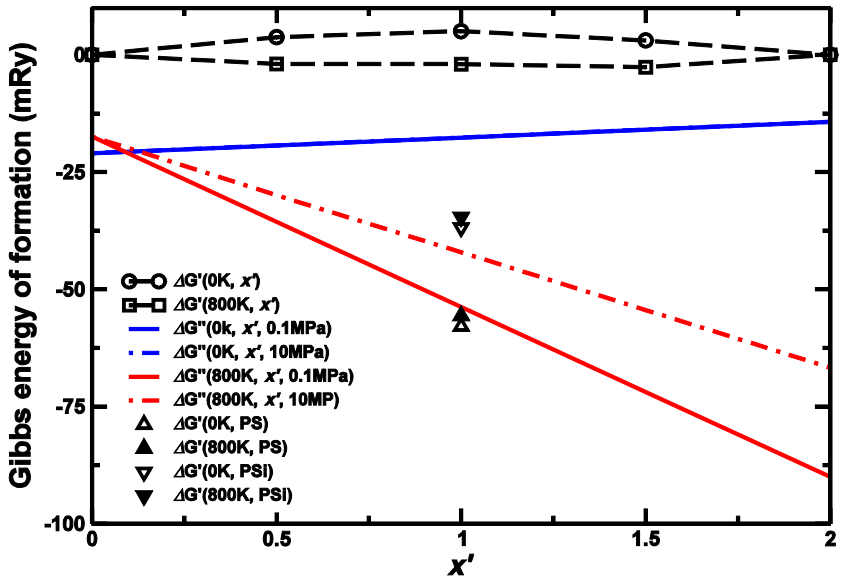

Figure 3.3 Comparison between the Gibbs energies $\Delta G'(T, x', 0.2)$ (dashed lines), $\Delta G'(T, \mathrm{PS}, 0.2)$ (upper triangles) and $\Delta G'(T, \mathrm{PSi}, 0.2)$ (lower triangles) calculated for $Sc_{0.5}Al_{0.4}Mg_{0.1}H_{x'}$. Results for $\Delta G''(T, x', 0.2, p_{H_2})$ are shown for pressures 100 kPa (solid lines) and 10 MPa (dashed-dotted lines). Energies refer per total number of Sc plus Al atoms and are given for temperatures 0 K and 800 K.

The Gibbs energy of formation for the phase separated PS and PSi systems at $x = 0.2$ is shown in Figure 3.3 by upper and lower triangles, respectively. At 0 K and $x = 0.2$ ($x = 0$), the PS system is found to be around 62.9 mRy (65.8 mRy) and the PSi around 41.9 mRy (44.8 mRy) more stable than the disordered CaF_2 phase at $x' = 1$. In general, the Gibbs energy of PS and PSi phases slightly decreases with Mg addition.

Figure 3.4 shows the critical temperatures below which the chemical reaction (3.1) is calculated to be exothermic. The upper panel in Figure 3.4 shows the critical temperatures for the PS system (T^{PS}) and the lower panel for the PSi system at two hydrogen partial pressures 100 kPa and 10 MPa as a function of Mg content. According to our results, the critical temperatures are above ~ 370 K; the ScH_2 plus $Al_{1-x}Mg_x$ phase decomposition will start by forming ScH_2 nuclei

in the $Al_{1-x}Mg_x$ matrix. The thermodynamic barrier for this process is given by the PSi formation energy. If the initial temperature is above T^{PSi}, then only the grains with size larger than λ_{min} will be stable. Therefore, we consider that the T^{PSi} temperatures represent the upper bound where hydrogenation of $ScAl_{1-x}Mg_x$ can be started. The hydrogenated sample will remain stable up to T^{PS}, above which the hydrogen release starts. Comparing our results for the critical temperatures with the experimental results for alloys containing 20% Mg [56]. Experimentally during hydrogen absorption the hydrogen gas was around 10 MPa and the hydrogenation was completed at 670 K. Hydrogen was released at 750 K at atmospheric pressure. According to Figure 3.4 at 20% Mg ($x = 0.2$), the hydrogen absorption temperature at 10 MPa is ~ 600 K and hydrogen release temperature at 100 kPa is ~ 805 K, we have to take into account the error bar which is ~ 50 K. We can say that the above results agree well with the experimental results.

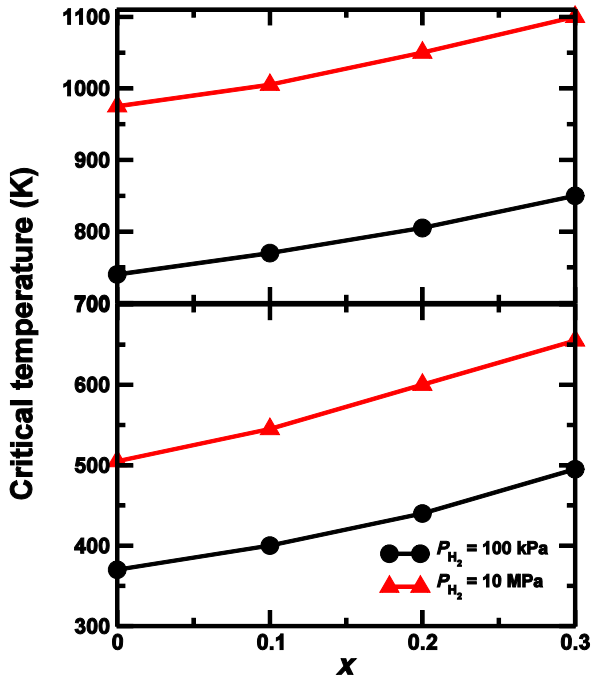

Figure 3.4 Theoretical critical temperatures below which the phase separated PS (upper panel) and the PSi (lower panel) ScH_2 plus $Al_{1-x}Mg_x$ system are thermodynamically stable with respect to $ScAl_{1-x}Mg_x$ plus hydrogen gas. The temperatures are plotted as a function of Mg content (x) and hydrogen pressure (p_{H_2}).

Chapter 4

Bain Path of Paramagnetic Fe-Cr-M (M=Cr, Mn, Co and Ni) Alloys

In this chapter we will discuss the alloying effects on the calculated total energies, the local magnetic moments and the softness of fcc and bcc lattices (against martensitic transformation) of the paramagnetic Fe-Cr-M (M = Cr, Mn, Co and Ni) alloys along the Bain path. For each system we performed calculations for seven different Wigner-Seitz (w) radius between 2.60 Bohr $\leq w \leq$ 2.75 Bohr and 14 different c/a ratios between 0.9 $\leq c/a \leq$ 1.55. The paramagnetic state of Fe-Cr-M alloys was simulated by the disordered local moments model. In the following sections we will present the main results of the above work.

4.1 Total Energy Maps

Figure 4.1 shows the total energy results for six different Fe-Cr based alloys as a function of Wigner-Seitz radius and c/a ratios, the energy shows a double-well structure with local minima at the cubic values of c/a (i.e. c/a =1 for bcc and $c/a = \sqrt{2}$ for fcc). We found that for all alloys the equilibrium radius is slightly larger (by less than ~1 %) in the bcc phase than in the fcc phase. This trend is typical for transition metals [57, 58]. From figure 4.1 we found that for $c/a < 1$ and $c/a > \sqrt{2}$ the total energy rises sharply making those bct lattices unstable.

According to our results for $Fe_{0.9}Cr_{0.1}$ in figure 4.1, we observed that at the equilibrium volume the fcc structure is more stable than bcc phase; the energy differences between the fcc and the bcc structures being $\Delta E \equiv E_{fcc} - E_{bcc} =$ -0.021 mRy per atom, for the energy barrier between the fcc and the bcc local minima (the energy barrier calculated for $c/a = 1.2$ and $w = 2.675$ Bohr), we obtained that $\Delta E_{fcc} \equiv E_{1.2} - E_{fcc} =$ 1.019 mRy (the barrier relative to the fcc structure) and $\Delta E_{bcc} \equiv E_{1.2} - E_{bcc} =$ 0.998 (barrier relative to the bcc structure). In these calculations we consider $Fe_{0.9}Cr_{0.1}$ as a reference and focus on the total energy of $Fe_{0.85}Cr_{0.1}M_{0.05}$ relative to the total energy of $Fe_{0.9}Cr_{0.1}$. We found that by adding 5 (10) % Cr to $Fe_{0.9}Cr_{0.1}$ the total energy differences increases by ΔE(Cr) = 0.443 (0.946) mRy in favour of the bcc structure and this result agrees well with observation in [59] and the energy barrier between the bcc and the fcc structure decreases to ΔE_{fcc} = 0.118 (0.276) mRy or relative to the bcc structure increases by ΔE_{bcc} = 0.325(0.670) mRy, and this mean that the energy minimum around the fcc phase is

shallower than that of $Fe_{0.9}Cr_{0.1}$ and deeper around the bcc phase. This supports the observation in Ref [60] that Cr decreases the tetragonal elastic constant of paramagnetic fcc $Fe_{0.9}Cr_{0.1}$. However, we observed that substituting 5 % Mn for Fe in the $Fe_{0.9}Cr_{0.1}$ alloy increases the energy differences between fcc and bcc relative to that of $Fe_{0.9}Cr_{0.1}$ by ΔE(Mn) = 0.045 mRy. According to this difference Mn slightly stabilizes the bcc structure. The energy barrier between

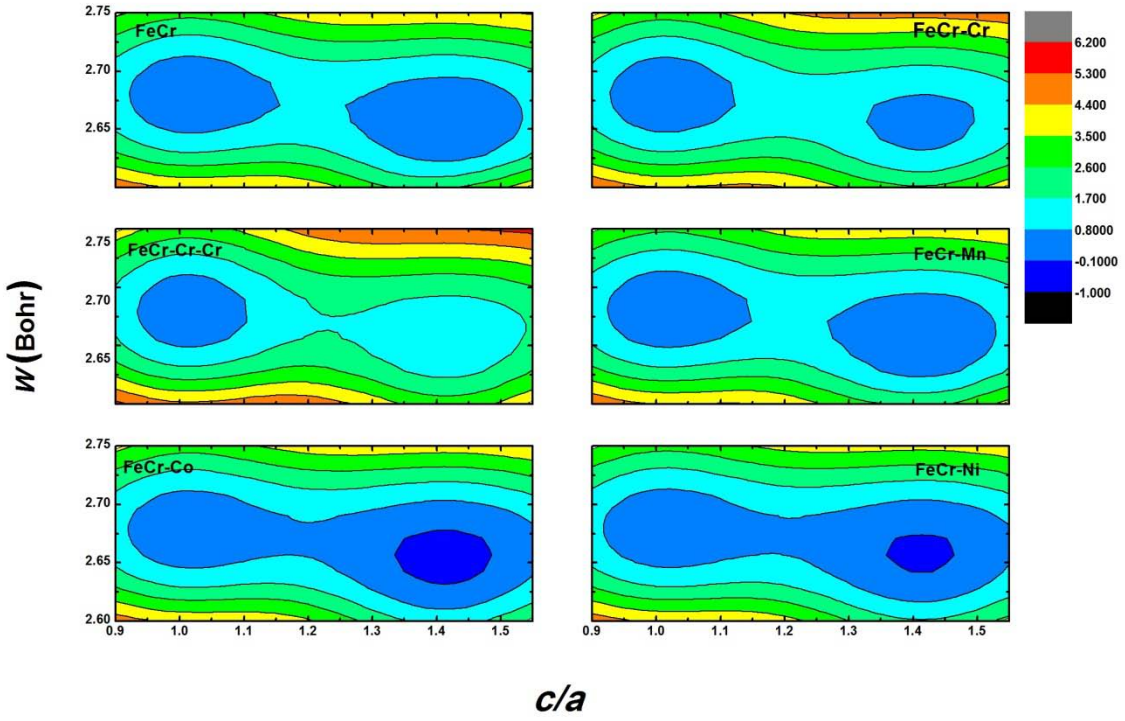

Figure 4.1 Total energy contours (in mRy) for Fe-Cr-M (M = Cr, Mn, Ni, Co) alloys as a function of the tetragonal lattice ratio *c/a* and the Wigner-Seitz radius (*w*). The energies are plotted relative to the minimum of the bcc (*c/a* = 1) total energy. The left panels from top to bottom are for $Fe_{0.9}Cr_{0.1}$ (FeCr), $Fe_{0.8}Cr_{0.2}$ (FeCr-Cr-Cr) and $Fe_{0.85}Cr_{0.1}Co_{0.05}$ (FeCr-Co), and the right panels from top to bottom for $Fe_{0.85}Cr_{0.15}$ (FeCr-Cr), $Fe_{0.85}Cr_{0.1}Mn_{0.05}$ (FeCr-Mn) and $Fe_{0.85}Cr_{0.1}Ni_{0.05}$ (FeCr-Ni), respectively.

these two cubic phases changes by approximately ΔE_f(Mn) = -0.025 mRy and ΔE_b(Mn) = 0.020 mRy. Nickel and Cobalt addition to $Fe_{0.9}Cr_{0.1}$ alloy yields ΔE(Ni) = -0.300 mRy, while ΔE(Co) = -0.451 mRy. The two metals additions to $Fe_{0.9}Cr_{0.1}$ strongly stabilize the fcc phase and this observation in line with [59]. On the other hand, Ni and Co change the energy barrier by ΔE_f(Ni) = 0.045 mRy or ΔE_b(Ni) = -0.255 mRy per atom and ΔE_f (Co) = 0.208 mRy per atom or ΔE_b (Co) = -0.243 mRy per atom relative to that of $Fe_{0.9}Cr_{0.1}$. Our energy barrier calculations of Ni

and Co are in contrast to those calculated for the elastic constants of paramagnetic Fe alloys in Ref [60].

We ascribe these effects of 3*d* transition metals addition to the $Fe_{0.9}Cr_{0.1}$ to the electronic mechanism and the changes of N_d upon alloying; the average *d*-occupation number for $Fe_{0.9}Cr_{0.1}$ is around 6.3 and this value is between Mn (5.5) and Fe (6.5). Therefore, Cr (4.5) addition decreases N_d while Co (7.5) and Ni (8.5) increases N_d. Manganese and iron have a negligible effect. According to the crystal structure theory of transition metals [61], for nonmagnetic solids with $4 \leq N_d \leq 6$ increasing (decreasing) *d*-occupation number stabilizes the fcc (bcc) phase. This observation was found for the nonmagnetic 3*d* metals in [61]. By using these changes with alloying, we found that the present energy differences are agreed with those in [61] and they obey to the simple crystal structure theory of transition metals [61]. On the other hand, by investigating the density of state of the above alloys around Fermi level, we found that for all systems the $D^{fcc}(\epsilon_F) > D^{bcc}(\epsilon_F)$. Furthermore, $D^{bcc}(\epsilon_F)$ increases with Mn and Co additions and slightly decreases with Cr and Ni additions, while $D^{fcc}(\epsilon_F)$ slightly increases (decreases) with Co (Cr) addition and strongly decreases with Ni addition and since increasing (decreasing) D (ϵ_F) might indicate that the center of gravity of the density of states is shifted towards larger (smaller) energies, and thus the one electron energy and kinetic energy increases (decreases). Therefore, the leading alloying effects on the kinetic energy are that Cr slightly stabilizes both fcc and bcc phases, Mn and Co strongly destabilizes the bcc phase, and Ni stabilizes the fcc phase.

4.2 The Alloying Effect on Softening the fcc and bcc Lattices of the Paramagnetic Fe-Cr-M (M = Cr, Mn, Co and Ni) Alloys

Figure 4.2 shows the calculated $\Delta E_{fcc}(c/a)$ (left panel) and $\Delta E_{bcc}(c/a)$ (right panel) as a function of alloying elements (M) for different c/a values. Here the energy differences are of the paramagnetic $Fe_{0.85}Cr_{0.1}M_{0.05}$ (M = Cr, Mn, Fe, Co and Ni) alloys relative to that $Fe_{0.9}Cr_{0.1}$ alloy. The tetragonal distortion (δ) around fcc or bcc lattice is given by the relation $c/a = (c/a)_{fcc\backslash bcc}/(1+\delta)^3$ [36] and the tetragonal elastic constant C' is directly related to the energy differences and δ at the equilibrium volume by the relation $\Delta E(\delta) = 6VC'\delta^2$ [36]. At specific δ, the C' is proportional to the energy differences.

From figure 4.2 (left panel) we observed that by adding 5 % Cr (Ni) to paramagnetic fcc $Fe_{0.90}Cr_{0.10}$, ΔE_{fcc} (1.35) is decreased by 0.008 (0.012) mRy relative to that of fcc $Fe_{0.90}Cr_{0.10}$. Here c/a = 1.35 corresponds to $\delta = 0.015$ distortion around the fcc phase, we expect that the tetragonal shear elastic constant of paramagnetic fcc $Fe_{0.90}Cr_{0.10}$ decreases too and this observation in line with that in [60]. This means that Cr (Ni) softens the fcc lattice. Cobalt addition to paramagnetic $Fe_{0.90}Cr_{0.10}$ increases ΔE_{fcc} (1.35) by 0.01 mRy, manganese has a small effect on the bct-fcc structural energy difference, which agrees with its negligible impact on C'_{fcc} [60]. For large distortions ($0.055 \geq \delta \geq 0.027$, *i.e.*$1.30 \geq c/a \geq 1.20$) ΔE_{fcc} (c/a) strongly increases (decreases) by adding Co (Cr). Nickel decreases the ΔE_{fcc} (c/a) energy difference for c/a >1.20.

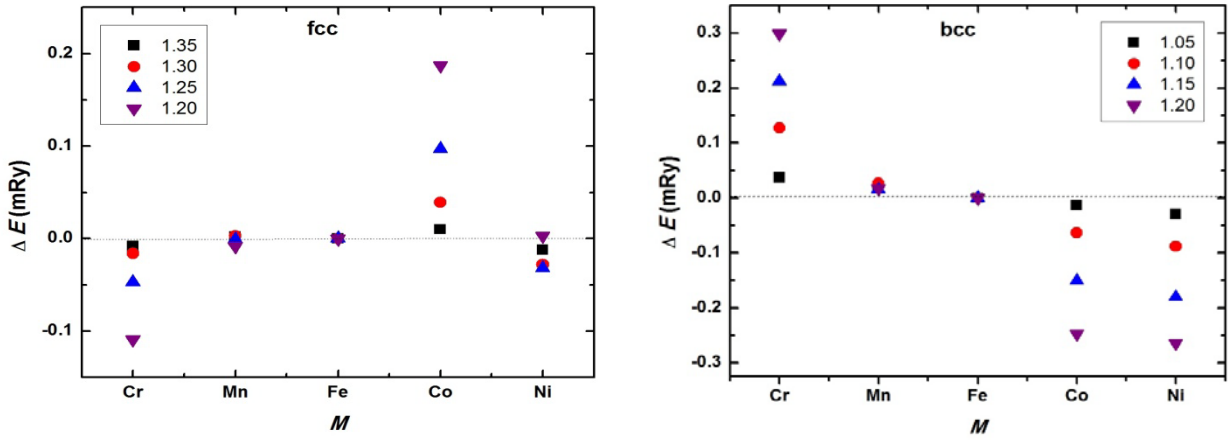

Figure 4.2 Theoretical energy differences between the bct and fcc (left panel) and between the bct and bcc phases (right panel) of the paramagnetic $Fe_{0.85}Cr_{0.10}M_{0.05}$ (M = Cr, Mn, Fe, Co, Ni) random alloys plotted relative to that of $Fe_{0.90}Cr_{0.10}$ as a function transition metal M possessing increasing *d*-occupation number as going from left (Cr) to right (Ni) and for different c/a ratios (distortions).

It is shown that by substituting 5 % Co (Ni) for Fe in paramagnetic bcc $Fe_{0.90}Cr_{0.10}$ (right panel in Figure 4.2), ΔE_{bcc} (c/a = 1.05) is decreased by 0.013 (0.03) mRy relative to that of bcc $Fe_{0.90}Cr_{0.10}$. This c/a =1.05 corresponds to distortion $\delta = 0.016$ around bcc lattice, the shear elastic constant of paramagnetic bcc $Fe_{0.90}Cr_{0.10}$ decreases too which means that Co and Ni soften bcc lattice. Chromium and Manganese have hardening effect on bcc lattice; adding 5 % of Cr (Mn) to the bcc $Fe_{0.90}Cr_{0.10}$ increases ΔE_{bcc} (1.05) by 0.037 (0.018) mRy. By increasing the

distortion to δ= 0.059 (i.e. c/a =1.20) the above trends become more pronounced, but Mn has a negligible effect even at large distortion.

4.3 The Magnetic Properties of Fe-Cr-M (M = Cr, Mn, Co and Ni) Alloys

Using DLM model to describe the paramagnetic phase of FeCrM (M = Cr, Mn, Co and Ni) alloys, we observed that the local magnetic moments on Fe atoms along the Bain path have the same trend in all alloys as shown in figure 4.3; at the same volume the local magnetic moments on Fe atoms have the maximum value at $c/a = 1$ (i.e. at bcc structure), while the minimum value at $c/a = \sqrt{2}$ (i.e. at fcc structure). On the other hand, the local magnetic moments on Fe atoms increase with increasing the Wigner-Seitz radius (w).

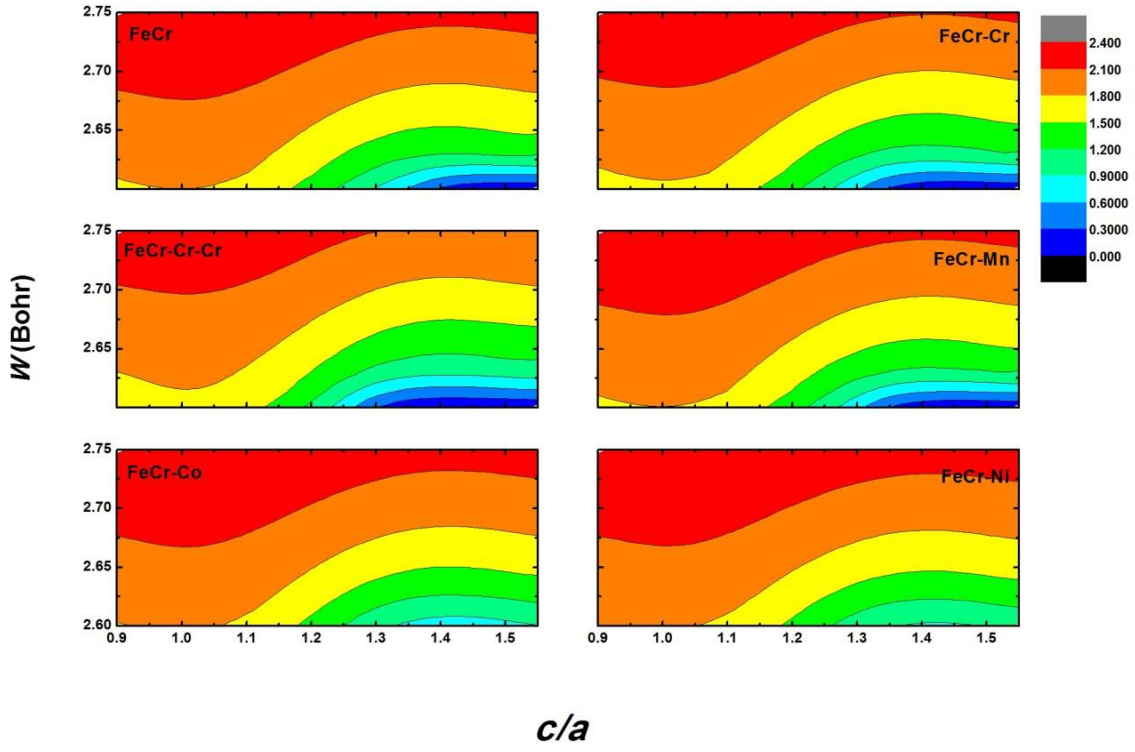

Figure 4.3 The local magnetic moments on Fe atoms of paramagnetic FeCrM (M = Cr, Mn, Ni, Co) alloys as a function of Wigner-Seitz radius *w* and tetragonal lattice ratio *c/a*.

The magnetic moments on Fe atoms for $Fe_{0.9}Cr_{0.1}$ alloy at equilibrium volume are 1.51 μ_B, we found that by substituting 5 % Cr (Mn) for Fe in $Fe_{0.9}Cr_{0.1}$ the magnetic moments on Fe atoms are decreased by 0.099 (0.038) μ_B. However, Co and Ni addition increases the magnetic

moments on Fe atoms by 0.033 (0.1) μ_B. The local magnetic moments on Cr atoms for $Fe_{0.9}Cr_{0.1}$, $Fe_{0.9}Cr_{0.15}$ and $Fe_{0.9}Cr_{0.20}$ and $Fe_{0.85}Cr_{0.1}Ni_{0.05}$ are vanished for the whole c/a and w range considered here. Cobalt has no local magnetic moments for $c/a > 1.30$ and Mn magnetic moments have almost constant values along the Bain path.

We investigated the magnetic entropy ($T\Delta S^{mag}$) for T = 1400 K using the mean-field approximation [62] and the free energy difference (ΔF^{mag}) between the fcc and bcc lattices for all systems. Results are shown in Table 4.1.

Table 4.1 Theoretical (EMTO-PBE) total energy, magnetic entropy and free energy differences between fcc and bcc phases of paramagnetic Fe-Cr-M (M = Cr, Mn, Co, Ni) alloys (in units of mRy) calculated at T = 1400K.

System	ΔE	$T\Delta S^{mag}$	ΔF^{mag}
$Fe_{0.90}Cr_{0.10}$	-0.021	-1.731	1.710
$Fe_{0.85}Cr_{0.15}$	0.412	-1.847	2.259
$Fe_{0.85}Cr_{0.1}Mn_{0.05}$	0.024	-1.850	1.874
$Fe_{0.85}Cr_{0.1}Co_{0.05}$	-0.474	-1.872	1.398
$Fe_{0.85}Cr_{0.1}Ni_{0.05}$	-0.321	-1.406	1.085

We found that for all alloys the magnetic entropy stabilize the bcc phase. This observation agree well with that in [63] in the case of Fe-Cr-Ni alloys, even though the free energy differences relative to that of $Fe_{0.90}Cr_{0.10}$ show that Co and Ni are fcc stabilizers. On the other hand, if we compare the energy differences with and without the magnetic entropy, we find that the energy difference of Fe-Cr-Co system reduces from 0.453 mRy (without $T\Delta S^{mag}$) to 0.312 mRy (with $T\Delta S^{mag}$) and that of Fe-Cr-Ni increases from 0.300 mRy (without $T\Delta S^{mag}$) to 0.625 mRy (with $T\Delta S^{mag}$), meaning that at high temperature Ni is a stronger fcc stabilizer than Co.

Conclusions and future work

In the present thesis we have investigated the proper basis set of the exact muffin-tin orbitals by calculating the equation of state for Al, Cu and Rh in two equivalent crystal lattice: the first one is the conventional face-centered-cubic lattice (str-I) and the second is the face-centered-cubic lattice with one atomic and three empty interstitial sites per primitive cell (str-II). For the fcc lattice, the *spd* basis for Al and the *spdf* basis for Cu and Rh yields accurate equilibrium properties, while for str-II Cu and Rh at least five orbitals (*spdfg*) are needed to get converged equilibrium properties. The muffin-tin potential sphere radius dependence of the calculated properties for str-II has been examined too; we found that for Al $S_{\mathrm{Al}} = 1.00 w_{\mathrm{Al}}$ and for Rh $S_{\mathrm{Rh}} = 1.10 w_{\mathrm{Rh}}$ are needed to get good representation of the full potential. For the Cu with 3*p* in the core, the best potential sphere radius is estimated to be around $1.07 w_{Cu}$, while when the 3*p* is treated to be as valence states, $S_{\mathrm{Cu}^*} = 1.10 w_{\mathrm{Cu}^*}$ yields accurate bulk properties.

As an application of the above work we have calculated the Gibbs energies of the $(\mathrm{Sc}_{0.5}\mathrm{Al}_{(1-x)/2}\mathrm{Mg}_{x/2}\mathrm{H}_{x'})$ random alloys in the CaF_2 structure, the $\mathrm{ScAl}_{1-x}\mathrm{Mg}_x$ quasi-random alloys in the CsCl structure and the phase separated system. For the phase separated system we considered two cases: the first was a fully separated bulk ScH_2 plus bulk $\mathrm{Al}_{1-x}\mathrm{Mg}_x$ (PS) and the second was ScH_2 and $\mathrm{Al}_{1-x}\mathrm{Mg}_x$ separated by interfaces of finite size (PSi). We demonstrated that adding Mg to the Al sublattice increases the stability of the hydrogenated alloys. At ambient pressure, the complete phase separated system remain stable up to 740 K at 0% Mg and 850 K at 30% Mg. The phase separated system with finite grain size lowered the above critical temperatures to 370 K and 495 K, respectively. The energetic of the hydrogenation reaction is very sensitive to the actual chemical composition of the parent alloy and to the structure of the hydrogenated solid.

The alloying effects of the paramagnetic Fe-Cr-M (M = Cr, Mn, Co, Ni) alloys were investigated by calculating the total energy differences, the local magnetic moments along the Bain path using EMTO-CPA-DLM approach. We demonstrated that Ni and Co addition stabilize the fcc phase, while Cr addition stabilizes the bcc phase. Manganese is predicted to be a very weak bcc stabilizer. The local magnetic moments on Fe atoms have minimum values for the fcc and maximum for the bcc structure, and they vanish on Cr and Ni atoms for the whole *c/a* and *w*

range considered here. Cobalt has no local magnetic moments for $c/a > 1.30$ while the Mn moments have almost constant values along the Bain path. Cobalt and Nickel are predicted to soften bcc lattice, while Ni and Cr are predicted to soften fcc lattice.

In the future, we will to continue working on the steel project by inserting carbon in interstitial sites of the paramagnetic Fe-Cr-M (M stands for Cr, Mn, Co and Ni) systems and investigate the fundamental physical properties of carbon containing steels.

Bibliography

1. N. W. Ashcroft and N. D Mermin: *Solid state physics*, Saunders College (1976).
2. R. A. H. Niessen, P. H. L. Notten, J. Alloys Comp. **877**. 293-295 (1999).
3. L. Schlapbach, A. Zuttel, Nature **414**, 353 (2001).
4. W. C. Leslie: *The Physical Metallurgy of Steels*, University of Michigan (1982).
5. A. V. Granato. Phys. Rev. Lett. **68,** 974 (1992).
6. M. Forsblom and G. Grimvall. Phys. Rev. B **72**, 054107 (2005).
7. K. Nordlund, Y. Ashkenazy, R. S. Averback, and A. V. Granato. Europhys. Lett. **71**, 625 (2005).
8. J. M. Ogden. Int J Hydrogen Energy, **24** (1999). 709-30.
9. B. Sakintuna, F Lamari.Darkrim, M. Hirscher. Int J Hydrogen Energy, **32** (2007), 1121-1140.
10. R. C. Weast, M. J. Astle, W. H. Beyer. CRC handbook of chemistry and physics. 64th ed., Boca Raton, FL: CRC Press; 1983.
11. M. L. Trudeau. MRS Bull, **24** (1999). 23-6.
12. W. P. Kalisvaart, R. A. H. Niessen, P. H. L. Notten, J. Alloys Comp. **417**, 280 (2006).
13. G. Sandrock, J. Alloys Comp. **877**. 293-295 (1999).
14. C. Zlotea, M. Sahlberg, P. Moretto, Y. Andersson, J. alloys Comp.**489**, 375 (2010).
15. P. Selvam, B. Viswanathan, C. S. Swamy and V. Srinivasan Int. J. Hydrogen Energy **11**, 169 (1986).
16. Z. Nishiyama. Science Repts. Tohoku Imp. Univ. **18**. 341-57(1928).
17. G. Wassermann. Arch. Archiv fuer das Eisenhuettenwesen **6**. 347-51(1933).
18. G. Kurdjumow and G. Sachs. Zeitschrift fuer Physik **64.** 325 -43 **(**1930).
19. E. C. Bain and N. Y. Dunkiri. Trans. Am. Inst. Min. Metal. Eng. **70.** 25 (1924).
20. R. M. Marten, *´´Electronic structure: Basic theory and practical methods´´*, Cambridg university press, (2004).
21. M. Born, K. Huang: *Dynamical theory of crystal lattices*, Oxford University press, Oxford, (1954).
22. P. Hohenberg and W. Kohn: Phys. Rev. **136B,** 864 (1964).
23. W. Kohn, and L. J. Sham: Phys. Rev. **140**, A 1133 (1965).
24. L. Hedin, B. I. Lundqvist, J. Phys. Chem. **4**, p. 2064 (1971).

25. J. C. Slater, Phys. Rev. **81**, p. 385 (1951).
26. J. P. Perdew, K. Burke, M. Ernzerhof: *Phys. Rev. Lett.***77**, 3865 (1996).
27. J. P. Perdew, A. Ruzsinszky, G. I. Csonka, O. A. Vydrov, G. E. Scuseria, L. A. Constantin, X. Zhou, and K. Burke, *Phys. Rev. Lett*. **100**, 136406 (2008); see also the supplementary information.
28. J. Korringa, Physica (Amsterdam) **13**, 392 (1947).
29. W. Kohn and N. Rostoker, Phys. Rev. **94**, 1111 (1954).
30. L. Szunyogh, B. Ujfalussy, P. Weinberger, and J. Kollár, Phys. Rev. B **49**, 2721 (1994).
31. H. L. Skriver, *The LMTO Method* (Springer-Verlag, Berlin, 1984).
32. O. K. Andersen, O. Jepsen, and M. Sob, in *Linearized Band Structure Methods*, Lecture Notes in Physics: Electronic Band Structure and Its Applications, edited by M. Yussouff (Springer Verlag, Berlin, 1987).
33. J. Kübler, *Theory of Itinerant Electron Magnetism* (Clarendon Press, Oxford, 2000).
34. O. K. Andersen, A. V. Postnikov, and S. Y. Savrasov, in *Applications of Multiple Scattering Theory in Materials Science*, edited by W. H. Butler, P. H. Dederichs, A. Gonis, and R. L.Weaver (Materials Research Society, Pittsburgh, PA, 1992).
35. O. K. Andersen, O. Jepsen, and G. Krier, *Lectures on Methods of Electronic Structure Calculation* (World Scientific, Singapore, 1994), p. 63.
36. L. Vitos. *The EMTO Method and Applications, in Computational Quantum Mechanicals for Materials Engineers* (London: Springer-Verlag, 2007).
37. L. Vitos, I. A. Abrikosov, B. Johansson. Phys. Rev. Lett. **87**, 156401 (2001).
38. L. Vitos, Johansson. B, J. Kollar and H. L. Skriver, Phys. Rev. B **62**, 10046 (2000).
39. L. Vitos, H. L. Skriver, B. Jöhansson, and J. Kollar, comput. Mater. Sci. **18**, 24 (2000).
40. L. Vitos, Phys. Rev. B **64**, 014107 (2001).
41. D. M. Ceperley, B. J. Alder. Phys. Rev. Lett. **45**, 566 (1980).
42. L. Vitos, J. Kolla'r, H. L. Skriver. Phys. Rev. B **55**, 13521 (1997).
43. L. Vitos, J. Kolla'r, H. L. Skriver Phys. Rev. B **49**, 16694 (1994).
44. L. Vitos, J. Kolla'r, H. L. Skriver Phys. Rev. B **49**, 11288 (1994).
45. J. Perdew, Y. Wang: Phys. Rev. B **45**, 13244 (1992).

46. J. Kollar, L. Vitos, H. L. Skriver.: From ASA Towards the Full Potential. In: Dreysse, H. (ed.) Lecture Notes in Physics: Electronic structure and Physical Properties of Solids. Springer-Verlag, Berlin Heidelberg New York Tokyo (2000).
47. P. Soven.: Phys. Rev. **156**, 809 (1967).
48. D. W. Taylor.: Phys. Rev. **156**, 1017 (1967).
49. B. L. Györffy.: Phys. Rev. B **5**, 2382 (1972).
50. D. A. Young, *Phase Diagrams of the Elements* (University of California Press, Berkeley, CA, 1991).
51. For the Debye temperatures of $Sc_{0.5}Al_{0.5}H_2$, $Sc_{0.5}Al_{0.5}$ and $Sc_{0.5}Al_{0.5}H$ in CaF_2 structure we obtained 360 K, 356 K and 351 K, respectively. For the Debye temperatures of $Sc_{0.5}Al_{0.5}$ in fcc structure and ScAl in CsCl structure we obtained 358 K and 379 K, respectively.
52. C. G. Van de Walle and J. Neugebaur Phys. Rev. Lett. **88**, 066103 (2002).
53. K. G. Nakamura, K. Ishioka, M. Kitajima, A. Endou, M. Kubo, and A.Miyamoto J. Chem. Phys. **108**, 3222 (1998).
54. C. Kittel and H. Kroemer, *Thermal Physics*, 2nd edition, Kingsport Press (1980).
55. S. Glasstone, *Thermodynamics for Chemists*, New York, D. van Nostrand Company (1947).
56. M. Sahlberg, P. Beran, T. K. Nielsen, Y. Cerenius, K. Kadas, M. P. J. Punkkinen, L. Vitos, O. Eriksson, T. R. Jensen, Y. Andersson, J. Solid State Chem. **182.** 3113 (2009).
57. A.G. Khachaturyan. *Theory of Structural Transformation in Solids* (New York: Wiley, 1983).
58. L. Vitos, J. Kollar. Phys. Rev. B **51**, 4074 (1995).
59. J. R. Davis, Davis and associates. *ASM Specialty Handbook: Stainless Steels*, Materials Park, OH (1994).
60. H. Zhang, N. Al-Zoubi , B. Johansson, and L. Vitos. (Unpublished).
61. H. L. Skriver: Phys. Rev. B **31,** 1909 (1985).
62. Grimvall G. Phys. Rev. **B** 39, 12300(1989).
63. Pitkänen H, Alatalo M, Puisto A, Ropo M, Kokko K, Punkkinen MPJ, Olsson P, Johansson B, Hertzman S, and Vitos L. Phys. Rev. B **79**, 024108 (2009).